Acoustic Doppler velocity measurement system using capacitive micromachined ultrasound transducer array technology

Minchul Shin and Joshua S. Krause
Department of Mechanical Engineering, Tufts University, Medford, Massachusetts 02155

Paul DeBitetto
Draper Laboratory, 555 Technology Square, Cambridge, Massachusetts 02139

Robert D. White[a)]
Department of Mechanical Engineering, Tufts University, Medford, Massachusetts 02155

This paper describes the design, fabrication, modeling, and characterization of a small (1 cm^2 transducer chip) acoustic Doppler velocity measurement system using microelectromechanical systems capacitive micromachined ultrasound transducer (cMUT) array technology. The cMUT sensor has a 185 kHz resonant frequency to achieve a 13° beam width for a 1 cm aperture. A model for the cMUT and the acoustic system which includes electrical, mechanical, and acoustic components is provided. Furthermore, this paper shows characterization of the cMUT sensor with a variety of testing procedures including Laser Doppler Vibrometry (LDV), beampattern measurement, reflection testing, and velocity testing. LDV measurements demonstrate that the membrane displacement at the center point is 0.4 nm/V^2 at 185 kHz. The maximum range of the sensor is 60 cm (30 cm out and 30 cm back). A velocity sled was constructed and used to demonstrate measureable Doppler shifts at velocities from 0.2 to 1.0 m/s. The Doppler shifts agree well with the expected frequency shifts over this range. © 2013 Acoustical Society of America.
[http://dx.doi.org/10.1121/1.4812249]

I. INTRODUCTION

Velocity measurement systems and rangefinders are used in a variety of applications, such as mobile robot positioning, personal navigation systems, micro air vehicle navigation, obstacle detection, and map building.[1–6] A number of approaches exist. Among suitable techniques, RADAR-based Doppler velocity or distance measurement systems in the 10 to 100 GHz band are often used. These systems include continuous wave (CW) systems for velocity measurement, and frequency modulated systems for distance measurement. However, RADAR based systems may require high power consumption and a large aperture to achieve a narrow beam width.

Acoustic rangefinders using piezoelectric actuation schemes are an alternative to radio frequency (RF) devices.[7] However, piezoelectric sensors operating in thickness mode (d_{33}) experience a limited acoustic impedance match to air, which provides poor effective transduction between the mechanical and acoustical fields. The deposition of matching layers or the careful design of bending structures using d_{31} mode coupling can increase efficiency.[8,9] Piezoelectric acoustic devices designed in this manner are effective, but may require large actuation voltages. In addition, piezoelectric materials can be expensive and difficult to fabricate as quality thin films when using a microelectromechanical systems (MEMS) based approach. Recent advances in the

fabrication and use of aluminum nitride films show promise for addressing these challenges, as well as providing better process compatibility.

In this work, we explore MEMS acoustic ultrasonic transducers for in-air velocity Doppler velocity measurement. Limited prior work has been described for MEMS transducer systems applied to in-air acoustic range finding and Doppler velocity measurement. In 2010, Przybyla *et al.* described a MEMS based piezoelectric acoustic rangefinder in air.[9] Przybyla *et al.* employed a thin film aluminum nitride membrane in a pulse-echo range finding configuration. In the current work, a significantly different approach is taken; a capacitive micromachined ultrasound transducer (cMUT) array is used in a CW mode for velocity measurement.

The array described here has many similarities to other cMUT devices, which were first described by Haller and Khuri-Yakub,[10,11] and have since been developed by a number of authors.[12–17] However, the majority of cMUT work has been directed toward biomedical ultrasound or submerged ultrasound. This paper presents the first demonstration of cMUT based in-air Doppler ultrasound.

The focus of this paper is to describe the design, fabrication, modeling, and characterization of a 1 cm^2 planar array. The sensor array has a 185 kHz resonant frequency to achieve a 13° beam width. A model for the cMUT and the acoustic system which includes electrical, mechanical, and acoustic components is provided. Furthermore, this paper provides characterization of the cMUT sensor with a variety of testing procedures. Acoustic testing, Laser Doppler Vibrometry (LDV), beampattern testing, reflection testing,

[a)]Author to whom correspondence should be addressed. Electronic mail: r.white@tufts.edu

and velocity testing were used to characterize the performance of the sensors.

II. FABRICATION

The cMUT sensor array was fabricated using the MEMSCAP PolyMUMPs® process along with facilities at Tufts University in the Tufts Micro and Nano Fabrication Facility.

PolyMUMPs® is a foundry process that produces a thin film polysilicon structure using surface micromachining processes. Seven physical layers, including three structural, two sacrificial, and one metal layer are used in the process. The process is shown schematically in Fig. 1.

The fabrication procedure for the sensor begins with a silicon wafer with high phosphorus surface doping. Low pressure chemical vapor deposition (LPCVD) is utilized to deposit a 600 nm silicon nitride. After the deposition of silicon nitride, 500 nm thick polysilicon (the Poly 0 layer) is deposited for the building of the bottom electrode by using LPCVD, and then patterned by photolithography and plasma etching. After the bottom electrode layer is deposited, a 2 μm oxide sacrificial layer is deposited by LPCVD and annealed for 1 h at 1050 °C. This heavily dopes the Poly 0 layer. Subsequently, 750 nm deep dimples are etched in the phosphosilicate glass (PSG) using reactive ion etching (RIE). The anchor regions are then defined by lithography and RIE. Subsequently, 2 μm of polysilicon (Poly 1) is deposited by LPCVD and patterned in a similar fashion. This is the first structural layer.

After the deposition of the first structure layer, a second PSG layer (Oxide 2) with a thickness of 750 nm is deposited and patterned. For the sensor described here, Oxide 2 is completely removed. Following this, the second structure layer of polysilicon (Poly 2), with 1.5 μm thickness, is deposited by LPCVD and patterned by RIE. Both polysilicon layers are heavily doped with phosphorous by diffusion from the PSG layers. The diaphragm structure is constructed from both polysilicon layers for a total polysilicon thickness of 3.5 μm. The final step in the PolyMUMPS process is the deposition of a 500 nm thick layer of chrome/gold, which is patterned by liftoff. This layer is used for electrical interconnect and the bond pads.

After the chips return from the PolyMUMPs® foundry, the device is released by etching the sacrificial oxide using 4:1 Hydrofluoric Acid (49%):Hydrochloric Acid (37%) mixture for 150 min. Note that the addition of HCl to the release etch is critical. Without HCl, the etch rapidly attacks the polysilicon grain boundaries, dramatically increasing series resistance. After the release etch, one additional Au layer (2 μm thick) is deposited to reduce the resonant frequency of the sensor. The Au layer is deposited by sputtering through a shadow mask. Next, the chip is packaged in a ceramic dual in-line package (DIP) using epoxy and is wire bonded. A small amount of epoxy was used behind the chip to attach it to the package, but no epoxy was used around the sides of the chip or to cover the wire bonds, in order to limit the packaging induced stresses in the chip. In testing, the resonant frequency of a particular element was observed to increase from 175 kHz before packaging to 180 kHz, indicating that a small amount of tensile residual stress was introduced during packaging. The observed shift is acceptable, but further study would be needed if a large number of chips were to be produced. Figure 2 shows the schematic of the complete sensor. Tables I and II give the geometric and material properties of the sensor structure.

III. DESIGN AND MATHEMATICAL MODELING

The cMUT sensor array consists of an 8×8 pattern where the elements are arrayed on a 1.01 cm $\times$ 1.01 cm chip, as shown in Fig. 3. Every sensor is connected in parallel. There are two bonding pads along the bottom edge of the chip for electrical connection. The element center-to-center pitch is 1.1 mm. Packaging uses a ceramic DIP to which the MEMS array is wire bonded. The device was designed with
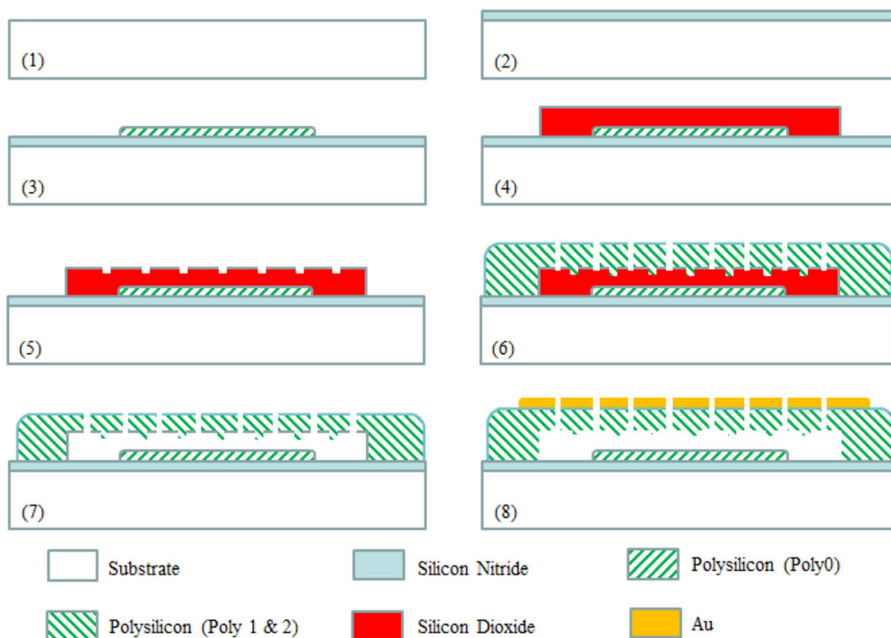

FIG. 1. (Color online) Schematic illustrating the fabrication process using the MEMSCAP PolyMUMPs® process. (1) Bare silicon substrate. (2) Silicon nitride layer is deposited as an electrical isolation layer. (3) Bottom electrode is patterned on the Poly 0 layer. (4) Sacrificial oxide layer is deposited to create the cavity. (5) Dimples are patterned into the first Oxide layer. (6) Poly 1 and Poly 2 layers are deposited and patterned as a diaphragm. (7) Oxide is removed through hydrofluoric acid release. (8) Au is deposited and sensor fabrication is complete.

Substrate	Silicon Nitride
Polysilicon (Poly 1 & 2)	Silicon Dioxide
Polysilicon (Poly0)	Au

Shin *et al.*: Micromachined Doppler ultrasound array chip

Poly0: phosphorus doped polysilicon, 500 nm thick
Metal: Cr/Au, 500 nm thick
Poly1 and Poly2: phosphorus doped polysilicon, 3.5 μm thick
Nitride: LPCVD silicon nitride, 600 nm thick
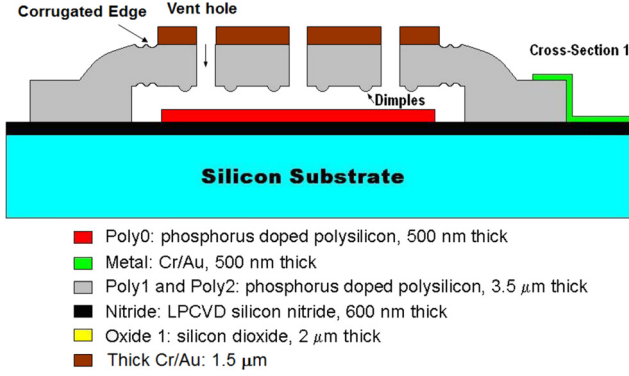**Oxide 1**: silicon dioxide, 2 μm thick
Thick Cr/Au: 1.5 μm

FIG. 2. (Color online) Schematic of one element in the cMUT sensor array showing the cross-sectional diagram after Au deposition.

a resonant frequency of 185 kHz, motivated primarily by the desire to achieve a 13° ($\pm$6.5° about center) -3 dB beam width (half power) with a 1 cm aperture. The beam width was chosen to be similar to commercial RF Doppler systems such as the Innosent IVS-167 (InnoSent GmbH, Donnersdorf, Germany). Based on stiction calculations[23] and previous experimental work with the PolyMUMPS process, the maximum achievable diaphragm diameter for the 3.5 μm thick polysilicon structure with a 2 μm air gap that could be fabricated without sticking down during release was 0.6 mm. However, this structure would have too high of a resonant frequency in air ($\sim$400 kHz). In order to bring the resonant frequency down to 185 kHz, 2 μm of gold was sputtered on in post processing.

The lumped element model shown in Fig. 4 was used for design calculations.[13,24] Figure 4 shows the lumped element model (LEM) for both the mechanical and electrical equivalent circuits. This model includes the sub-elements of the model: External environmental air loading, cMUT structural mechanics, electromechanical coupling, backing cavity compliance, air damping, and the negative electrostatic spring. The modeling procedure closely follows the methods described by Doody et al.[13] The most significant difference from the model of Doody et al. is that this device has holes through the diaphragm to front vent the device.

The environmental mass loading represents the acoustic radiation impedance of the vibrating diaphragm radiating into an infinite half-space. The mechanical radiation impedance of a circular diaphragm in an infinite baffle oscillating in the static clamped mode shape is approximated by Greenspan[25]

$$Z_{\text{mech}} \approx \frac{F}{U_{\text{dia}}} \approx \rho c \left(\frac{1}{2}(ka)^2 + \frac{2^9}{5^2 \cdot 7\pi} jka \right), \quad (1)$$

TABLE I. Geometric properties of the microphone.

Symbol	Property	Value	Units
a	Radius of diaphragm	300	μm
t_{poly}	Thickness of polysilicon layer	3.5	μm
t_{gold}	Thickness of gold layer	2.0	μm
a_{hole}	Radius of diaphragm vent holes	2.0	μm
n	Number of vent holes in diaphragm	28	

which is valid at low frequencies, where $ka \ll 1$. F is the total force from the area integral of pressure on the diaphragm, U_{dia} is the volume velocity of the diaphragm, ρ is the density of air, c is the speed of sound, a is the radius of the diaphragm, and k is the acoustic wavenumber. The result was derived for a circular diaphragm oscillating in a clamped static bending mode shape

$$u(r,t) = U_0 \left[1 - \left(\frac{r}{a} \right)^2 \right]^2 e^{j\omega t}, \quad (2)$$

where $u(r,t)$ is the oscillatory surface velocity of the diaphragm. The environmental acoustic impedance can be approximated by area averaging the force

$$Z_{\text{env}} \approx \frac{F}{AU_{\text{dia}}} \approx \frac{\rho c}{\pi a^2} \left(\frac{1}{2}(ka)^2 + \frac{2^9}{5^2 \cdot 7\pi} jka \right), \quad (3)$$

where $A = \pi a^2$ is the area of the diaphragm. This impedance can be represented as a parallel combination of an acoustic resistance and acoustic mass

$$Z_{\text{env}} = ((M_A j\omega)^{-1} R_A^{-1})^{-1}. \quad (4)$$

At low frequencies, for ka much less than 1, the values of the resistance and mass are

$$R_A = 0.551 \frac{\rho c}{a^2} \quad (5)$$

$$M_A = 0.296 \frac{\rho}{a}. \quad (6)$$

It may be possible to improve on this environmental impedance using more terms in the approximation, and other methods of averaging the pressure over the diaphragm to preserve power. The results of Greenspan[25] and Lax[26] are useful in this regard, particularly for systems that may be loaded by a heavy fluid where environmental impedance effects become

TABLE II. Material properties of the diaphragm.

Symbol	Property	Value	Units	Reference(s)
ρ_{poly}	Density of polysilicon	2320	kg/m^3	Madou (Ref. 18)
ρ_{gold}	Density of gold	19 300	kg/m^3	Bauccio (Ref. 19)
E_{poly}	Modulus of elasticity of polysilicon	160	GPa	Sharpe (Ref. 20)
E_{gold}	Modulus of elasticity of gold	80	GPa	Rashidian and Allen (Ref. 21)
v_{poly}	Poisson's ratio of polysilicon	0.22	Dimensionless	Sharpe (Ref. 20)
v_{gold}	Poisson's ratio of gold	0.44	Dimensionless	Gercek (Ref. 22)

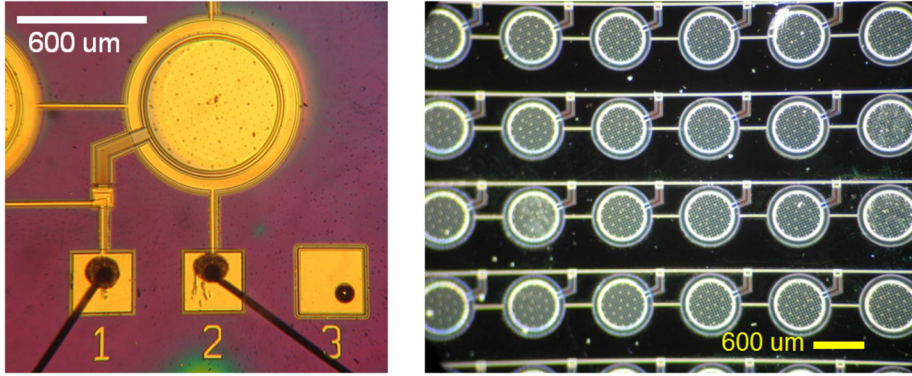Shin et al.: Micromachined Doppler ultrasound array chip 1013

FIG. 3. (Color online) Microscope image of a single element after packaging using light field illumination (left) and a portion of the cMUT array using dark field illumination (right).

dominant. However, for the system presented here which operates in air, the environmental impedance is not a dominant effect.

The damping from the air flowing through the vent holes and the air flowing laterally in the cavity is also shown in Fig. 4. The impedance is calculated as the sum of two dominant resistances: The resistance for flow through the holes, which comes from the classical small pipe resistance with end corrections, and the squeeze film damping for a perforated plate, estimated using Skvor's formula (S and C_f below).[24,27] Homentcovschi and Miles confirm and extend this result.[28]

$$R_{vent} = R_{hole} + R_{squeeze},$$ (7)

$$R_{hole} = \frac{8\mu}{n\pi a_{hole}^4}\left(t_{poly} + t_{gold} + \frac{3}{8}\pi a_{hole}\right),$$ (8)

$$R_{squeeze} = \frac{12\mu C_f}{n\pi t_{gap}^3},$$ (9)

$$C_f = \frac{S}{2} - \frac{3}{8} - \frac{S^2}{8} - \frac{1}{2}\ln(\sqrt{S}),$$ (10)

$$S = \frac{na_{hole}^2}{a^2},$$ (11)

where μ is the viscosity of air, t_{poly} is the thickness of the polysilicon, t_{gold} is the thickness of gold, n is the number of holes in the diaphragm, a_{hole} is the radius of the holes in the diaphragm, and S is the ratio of the open hole area to the total diaphragm area. Note that this resistive element is in parallel with the cavity compliance, and thus neglects additional squeeze damping that would be present due to air motion for compression in the backing cavity (which would be in series with the cavity compliance). It is assumed that the damping from flow to and through the diaphragm holes is dominant over flow due to nonuniform compression in the gap, due to the relatively large and closely spaced vent holes.

The cavity compliance represents the stiffness of the air in the backing cavity as it is compressed by the diaphragm during its deflection. C_{cav} is determined from the volume of the gap, V_{gap} divided by the product of the density of air, ρ, and the speed of sound, c, squared.

$$C_{cav} = \frac{V_{gap}}{\rho c^2}.$$ (12)
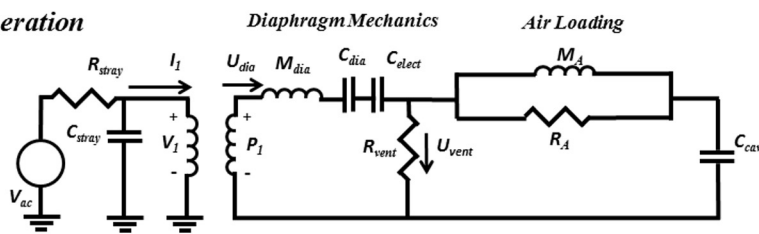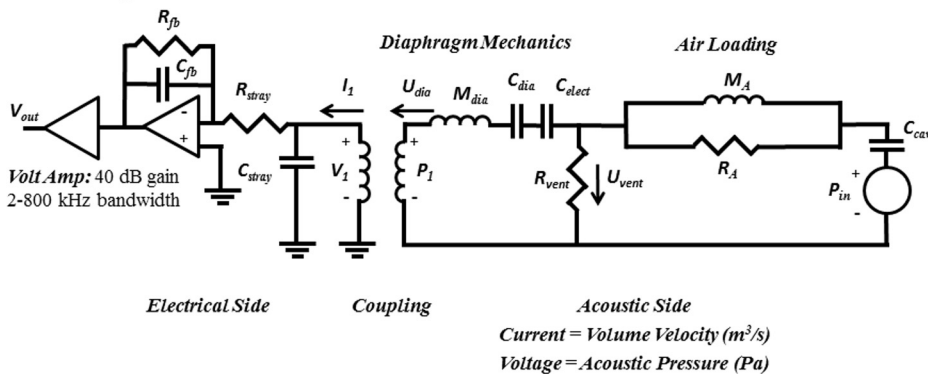
FIG. 4. Coupled mechanical-electrical lumped element model.

Shin *et al.*: Micromachined Doppler ultrasound array chip

The compliance of the diaphragm (for a two layer thin laminate clamped circular bending plate) with the effective bending stiffness of the gold layer and the polysilicon diaphragm, and the effective mass of the diaphragm (for the first mode of the same two layer thin laminate clamped circular bending plate) are computed using the classical thin laminate plate theory

$$C_{\text{dia}} = \frac{\pi a^6}{16 \cdot 12} \frac{1}{D_{\text{eff}}}, \tag{13}$$

$$D_{\text{eff}} = \sum_i \frac{E_i}{1 - \nu_i^2} \left(\frac{t_i^3}{12} + t_i y_i^2 \right), \tag{14}$$

$$y_c = \frac{\sum_i z_i \left(\frac{E_i t_i}{1 - \nu_i^2} \right)}{\sum_i \frac{E_i t_i}{1 - \nu_i^2}}, \tag{15}$$

$$y_i = z_i - y_c, \tag{16}$$

$$M_{\text{dia}} = \frac{9(\rho_{\text{poly}} t_{\text{poly}} + \rho_{\text{gold}} t_{\text{gold}})}{5 \pi a^2}, \tag{17}$$

where i is an index for the layer type (polysilicon or gold), y_c is the position of the neutral axis with respect to the bottom of the laminate, y_i is the distance from the center of the ith layer to the neutral axis, and z_i is the position of the center of the ith layer with respect to the bottom of the laminate. E_i, ν_i, t_i, and ρ_i are the elastic modulus, Poisson ratio, thickness, and density of the ith layer, respectively. D_{eff} is the effective bending stiffness of the laminate plate. M_{dia} and C_{dia} are the final results of the calculation, the effective diaphragm mass, and compliance.

The coupling from the mechanical to electrical side via the ideal transformer is shown in Eqs. (18) and (19) where P_1 is the effective electrostatic pressure, V_1 is the voltage across the electrodes, I_1 is the current flow through the capacitor, and U_{dia} is the volume velocity of the diaphragm.

$$P_1 = N \cdot V_1, \tag{18}$$

$$I_1 = N \cdot U_{\text{dia}}. \tag{19}$$

When operating in receive mode, the cMUT array is held at a constant dc bias, V_{bias}. When operating in transmit mode for electrostatic (laser vibrometry testing) a voltage $V(t) = V_{\text{bias}} + V_{\text{ac}} e^{j\omega t}$ is applied to the system. In these cases the coupling factor is

$$N = \frac{V_{\text{bias}} \varepsilon_0}{t_{\text{gap}}^2}. \tag{20}$$

In acoustic transmit mode, the cMUT array is driven with a pure ac drive, $V(t) = V_{\text{ac}} e^{j\omega t}$ and the coupling factor is

$$N = \frac{V_{\text{ac}} \varepsilon_0}{4 t_{\text{gap}}^2}, \tag{21}$$

where V_{ac} is the amplitude of the ac drive signal. In this case all mechanical signals in the linear LEM will be at twice the drive frequency. This frequency doubling effect is caused by the quadratic nature of the electrostatic coupling.

The electrostatic spring compliance is, when a dc bias is used,

$$C_{\text{elect}} = \frac{-t_{\text{gap}}^3}{V_{\text{bias}}^2 \varepsilon_0}, \tag{22}$$

or, in transmit mode with pure ac drive,

$$C_{\text{elect}} = \frac{-16 t_{\text{gap}}^3}{V_{\text{ac}}^2 \varepsilon_0}. \tag{23}$$

Modeling of the electrostatic coupling and the negative electrostatic spring follow the methods of Doody et al.[13] Two LEMs of a single cMUT element were used, as can be seen in Fig. 4. The top model shows the component in "transmit" mode. In this mode, the input voltage, V_{ac}, is driven on the left side of the model as a voltage source. The output of this mode is the diaphragm volume velocity, U_{dia} and vent hole volume velocity, U_{vent}. It is emphasized again that, for a pure ac voltage drive with zero dc bias, all mechanical quantities (such as diaphragm volume velocity) will be at twice the drive frequency due to the quadratic nature of the electrostatic coupling. It is possible to compute the pressure in the farfield by summing the baffled monopole fields transmitting from all of the array elements

$$P = j\rho f \cdot \sum_{m=1}^N \frac{1}{R_m} \cdot (U_{\text{dia}} - U_{\text{vent}}) e^{-jkR_m} H(\theta), \tag{24}$$

where $U_{\text{dia}} - U_{\text{vent}}$ is the net source volume velocity: The difference between the diaphragm volume velocity and the flow through the vent holes. These volume velocities are computed from the LEM of a single transducer, $k = \omega/c$ is the acoustic wavenumber, f is the transmit frequency in cycles/s, ρ is the density of air, and R_m is the scalar distance from the center of the mth array element to the field point. $H(\theta)$ is the directivity of an individual element. At the drive frequency of 185 kHz, ka is close to unity, so the individual elements are somewhat directional.

The beampattern of a baffled piston is used to approximate the beampattern of the individual elements,

$$H(\theta) = \frac{2 J_1(k a_{\text{eff}} \sin \theta)}{k a_{\text{eff}} \sin \theta}, \tag{25}$$

where θ is the angle, measured from the normal, to the field point, and J_1 is the Bessel function of the first kind, order 1. For the purposes of directivity calculation, the effective radius, a_{eff}, of the transmitting element should be used. Since the element deforms as a circular bending plate, the effective radius of an equivalent baffled piston is somewhat less than the physical radius. An effective radius equal to 70% of the physical radius is a good approximation. This was determined by a finite element computation of the beampattern projected into an infinite half space by a baffled clamped axisymmetric circular plate oscillating in the clamped static mode shape given in Eq. (2). The individual
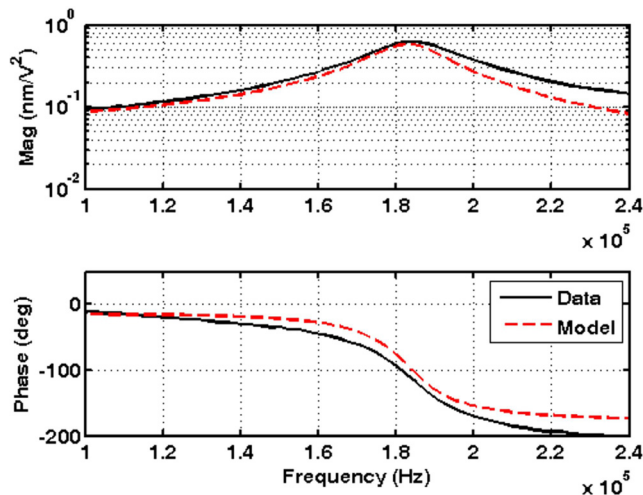
FIG. 5. (Color online) Predicted center point motion frequency response for a single element and the experimental result.

elements are not strongly directional at the frequency of operation, so the array beampattern is not strongly affected by small changes to the effective radius. The summation is over the 64 array elements. Since all the elements are identical, all the $U_{dia} - U_{vent}$ are the same, and only the distance to the field point, R_m, changes. This transmit model neglects any acoustic coupling between the elements.

The bottom picture shows the component in "receive" mode. In receive mode, an acoustic pressure, P_{in}, is delivered from the environment, vibrating the diaphragm of the receiver. The output of the receive mode is the current flowing on the electrical side, which is integrated by the charge amplifier to produce the measured voltage output. In the charge amplifier, C_{fb} is 150 pF and R_{fb} is 10 MΩ, resulting in a high pass filter cutoff of 5 kHz for the preamplifier stage. Following the charge amplifier, the signal is passed into a series of two operational amplifier based inverting amplifier circuits with single pole high pass filters. The second and third amplifier stages are based on the OP27 low noise operational amplifier (Analog Devices, Norwood, MA), each configured with a gain of 20 dB and a bandwidth of 2 to 800 kHz. The low frequency cutoff is determined by discrete components in the high pass filter design, and the high frequency cutoff is set by the gain bandwidth product of the amplifier in combination with the designed gain of 20 dB.

IV. EXPERIMENTAL RESULTS

To investigate the dynamic behavior of the sensor membranes, LDV was first used to test the electromechanical frequency response. The laser spot was directed to the center of each membrane. A frequency sweep was driven using a signal generator, with an applied dc bias and ac voltage. The vibratory displacement response of the cMUT sensor array was measured by LDV. A comparison between predicted frequency response results and measurement is shown in Fig. 5. The magnitude is normalized to the product of the applied dc bias and ac bias during electrostatic drive. This choice of normalization is made to emphasize that it is this product which is proportional to electrostatic force at the drive frequency. Measured frequency response by LDV is in excellent agreement with model predictions. As expected, the resonant frequency decreased to approximately 185 kHz after a 2 μm gold layer was deposited by shadow masking. Before the deposition of Au, the resonant frequency of the membrane is 430 kHz. All 64 elements in the array were measured in this fashion. For the transmitter chip, the average value of the resonant frequency of 64 elements is 180.26 kHz and the standard deviation is 3.97 kHz, with 61/64 element yield. The average phase at the peak is −113°, with a standard deviation of 5.2°. For the receiver chip, the average value of the resonant frequency of 64 elements is 193.74 kHz and the standard deviation is 3.69 kHz with 58/64 element yield. The average phase at the peak is −118° with a standard deviation of 7.3°. For both chips, the quality factor (Q) is 9.

Second, a free field acoustic beampattern measurement was conducted for the array relative to a reference microphone. As shown in Fig. 6, on the transmit side, a rotary positioner was used to incrementally rotate the cMUT transmit chip about its center. The beampattern, also shown in Fig. 6, was measured at 10 cm from the source (in the far field of the array, but still within the direct field), using a B&K $\frac{1}{4}$ in. free field microphone (Bruel and Kjaer, Denmark). The voltage drive to the cMUT was 20 V$_{peak-to-peak}$ at 40 kHz. Frequency doubling due to the electrostatic drive produced acoustics at 80 kHz. The measurement was conducted in CW operation at 80 kHz. This test was run below the designed operating frequency of the cMUT (185 kHz) because the B&K cannot measure above 100 kHz. Results show a beampattern very similar to model predictions. The measured
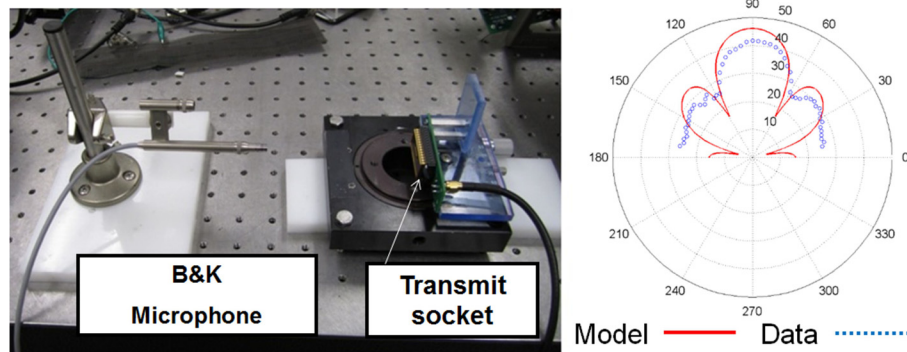

FIG. 6. (Color online) Acoustic transmit test using cMUT array (80 kHz). Experimental setup (left) and beampattern (right). Beampattern is in units of dB SPL.

1016   J. Acoust. Soc. Am., Vol. 134, No. 2, August 2013

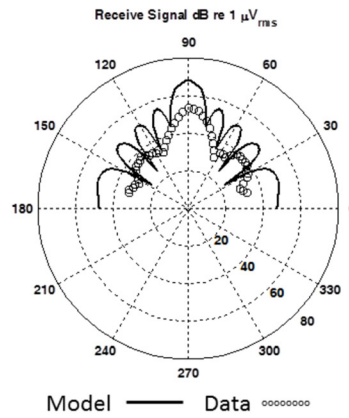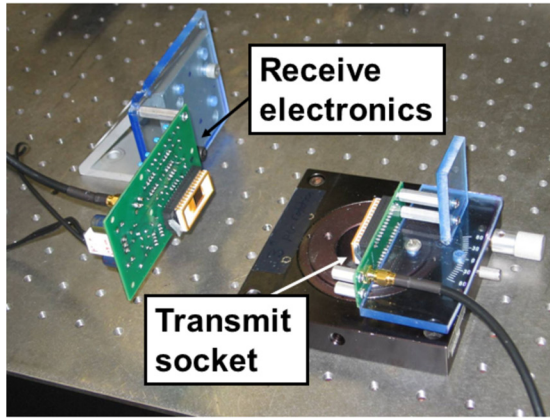Shin *et al.*: Micromachined Doppler ultrasound array chip

FIG. 7. (Color online) Acoustic transmit and receive testing using two cMUT arrays at 185 kHz. Experimental setup (left) and beampattern (right).

response was 40 dB sound pressure level (SPL) (re 20 μPa$_{rms}$) (rms = root-mean-square) at 10 cm on axis.

A second free field measurement was conducted using a pair of cMUT chips. The experimental setup and results are shown in Fig. 7. The transmit chip was driven electrically at 92.5 kHz drive with 20 V$_{peak-to-peak}$. Again, frequency doubling due to square law electrostatics gave acoustics at 185 kHz. This has the advantage of reducing electromagnetic interference (EMI) from direct RF transmission, which is primarily at 92.5 kHz. Driving at half frequency with pure ac is an effective and simply implemented method of reducing EMI contamination of the results. The transmitter was on the rotary positioner. The dc bias on the receiver was 10 V. The transducer arrays were 10 cm apart. The measured response was 0.5 mV$_{rms}$ (53 dB re 1 μV$_{rms}$) at peak, which compares reasonably well with the predicted 2.5 mV$_{rms}$ from the computational model. The discrepancy in absolute level could be due to a combination of factors including mismatches between the two array chips, imperfect alignment during testing, and scattering off of the test structures. The -3 dB beam width (half power) is as expected at 13° (6.5° on either side of the center). The side lobes are down by 15 dB compared to the main lobe.

To investigate the achievable range of a reflected acoustic wave, range testing with a reflecting boundary was conducted, as shown in Fig. 8. During range testing experiments, the angle of the transducers was adjusted at each distance D in order to maximize the return signal. The lateral distance between the array chips was 10 cm. There was an acrylic plate in between the arrays to prevent direct transmission between the chips. As in the previous experiment, the drive signal was 20 V$_{pp}$ at 92.5 kHz, and the dc bias on the receiver side was 10 V. Experimental results for reflected acoustic

CW transmit and receive using two chips reflecting off a flat aluminum plate show a maximum range of 60 cm (30 cm out and 30 cm back) as shown in Fig. 8. Signal power decreases with the square of D as expected. With $D \geq 30$ cm, the signal decreases below the noise floor (-91 dB V$_{rms}$). In this experiment, the sampling frequency was $F_s = 1$ MHz and the number of samples was 2,[21] resulting in a total data acquisition time of 4.2 s per point. The resulting noise bandwidth is 0.24 Hz.

Figure 9 shows a schematic of the preamplifier electronics including all electronic noise sources. The contributions to the total noise from each component in the electronics have been analyzed. Each noise source is uncorrelated, and so can be considered separately. Linear circuit theory, using an ideal op-amp model for the AD8065, can be applied to determine the transfer functions for each term. The total noise can be added in a rms sense. The various contributions to the total noise, at the AD8065 output, are

$$V_{e_{bias}} = \frac{-Z_{fb}C_{sensor}j\omega}{1 + R_{filt}(C_{filt} + C_{sensor})j\omega}e_{bias}, \tag{26}$$

$$V_{e_n} = \left(1 + \frac{Z_{fb}C_{sensor}j\omega(1 + R_{filt}C_{filt}j\omega)}{1 + R_{filt}(C_{filt} + C_{sensor})j\omega}\right)e_n, \tag{27}$$

$$V_{i_n} = Z_{fb}i_n, \tag{28}$$

$$V_{i_{fb}} = Z_{fb}i_{fb}, \tag{29}$$

where the feedback impedance is the parallel combination of the feedback components

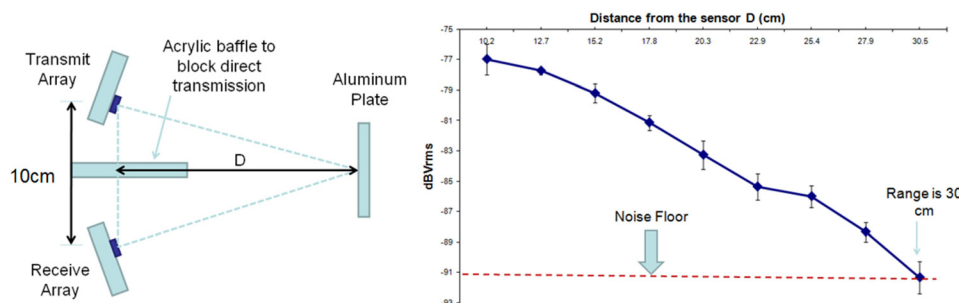$$Z_{fb} = \frac{R_{fb}}{1 + R_{fb}C_{fb}j\omega}. \tag{30}$$

FIG. 8. (Color online) Reflection test using cMUT array. Sensor signal is in dB V$_{rms}$ in a 0.24 Hz band (4.2 s averaging time).

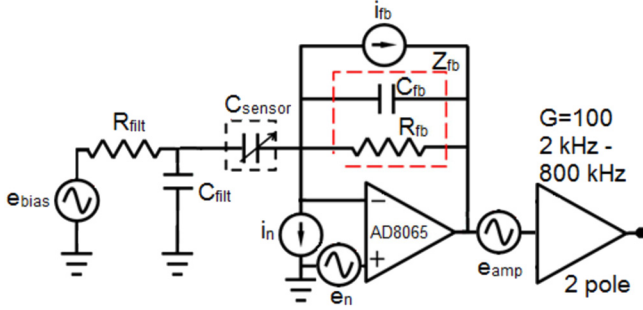Shin *et al.*: Micromachined Doppler ultrasound array chip   1017

FIG. 9. (Color online) Schematic of the preamplifier electronics including electronic noise sources.

TABLE III. Electrical elements in the noise model.

Symbol	Property	Value	Units
C_{sensor}	MEMS sensor capacitance	4	nF
R_{filt}	Filter resistor	1	kΩ
C_{filt}	Filter capacitor	10	μF
C_{fb}	Feedback capacitor	150	pF
R_{fb}	Feedback resistor	10	MΩ
f_1	Low frequency band limit for the bandpass filter	2	kHz
f_2	High frequency band limit for the bandpass filter	800	kHz
G	Gain of the bandpass filter	100	
k	Boltzmann constant	1.38×10^{-23}	J/K

The component values are given in Table III. The noise contributions are acted on by the transfer function of the two stage bandpass filter downstream of the AD8065. This bandpass filter is constructed using two OP27 operational amplifiers. The first of these amplifiers contributes additional noise, e_{amp}. The resulting noise densities add in an rms sense to produce the total noise density estimate at the output of the electronics

$$V_{out} = G\sqrt{V_{bias}^2 + V_{Ve_n}^2 + V_{i_{fb}}^2 + V_{i_n}^2 + e_{amp}^2}$$
$$\times \left| \frac{\frac{j\omega}{2\pi f_1}}{\left(1 + \frac{j\omega}{2\pi f_1}\right)\left(1 + \frac{j\omega}{2\pi f_2}\right)} \right|^2, \quad (31)$$

where G is the passband gain of the bandpass amplifier, f_1 and f_2 delineate the bandwidth of the bandpass filter, $i_{fb} = \sqrt{4kT/R_{fb}}$, is the Johnson noise from the feedback resistor, $e_{amp} = 3$ nV/$\sqrt{Hz}$ is OP27 voltage noise, $e_n = 7$ nV/$\sqrt{Hz}$, and $i_n = 0.6$ fA/$\sqrt{Hz}$, are the voltage and current noise from the AD8065, respectively. The values for e_{inst}, e_n, and i_n come from the data sheets (Analog Devices, Norwood, MA). Also according to the datasheet of the REF01 10 V reference IC (Analog Devices, Norwood, MA), the bias voltage noise has a low frequency noise density of 3 μV/$\sqrt{Hz}$, and exhibits a $1/f$ dependence at high frequencies. It is well modeled by

$$e_{bias} = (3 \, \mu V/\sqrt{Hz}) \frac{2\pi(10 \, kHz)}{2\pi(10 \, kHz) + j\omega}. \quad (32)$$

Figure 9 shows the contribution of each noise source and the rms total of the noise sources as a whole. As can be seen from Fig. 9, the system noise near the 185 kHz operating frequency is dominated by the voltage noise of the preamplifier chip. The noise model is directly compared to a measurement of the system output noise density in Fig. 10, with excellent agreement. This suggests that the major noise sources in the system have been captured. Voltage noise dominates current noise, bias noise, and thermal noise for this particular system, thus the noise density at the system output can be estimated from the preamplifier voltage noise amplified by the preamplifier gain and bandpass stage gain,[29]

$$e_{noise} = e_n \left| 1 + \frac{C_s}{C_{fb}} \right| G, \quad (33)$$

where $e_n = 7$ nV/$\sqrt{Hz}$ is the AD8065 voltage noise density, $C_s = 4$ nF is the sensor capacitance, $C_{fb} = 150$ pF is the feedback capacitance of the preamp, and $G = 100$ is the passband gain of the second and third stage amplifiers. This simple model results in an estimated noise floor of 20 μV/$\sqrt{Hz}$ at the system output, identical to the value measured near 185 kHz.

In the final set of tests, a velocity sled was constructed and used to demonstrate measureable Doppler shifts at velocities from 0.2 to 1.0 m/s. The velocity test setup consists of a speed controller, a dc motor, a shaft encoder, and a moving sled, as shown in Fig. 11. The transmitter faces the receiver. The tests were conducted with the transmitter moving and the receiver stationary, so no reflections were needed; this improved the signal-to-noise ratio. A continuous
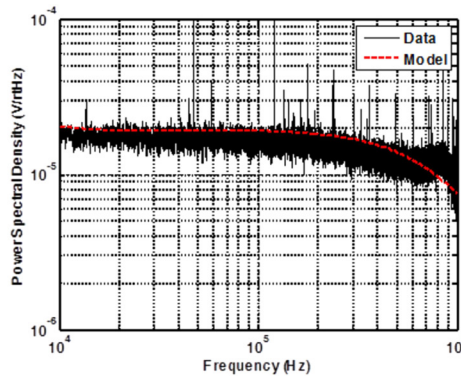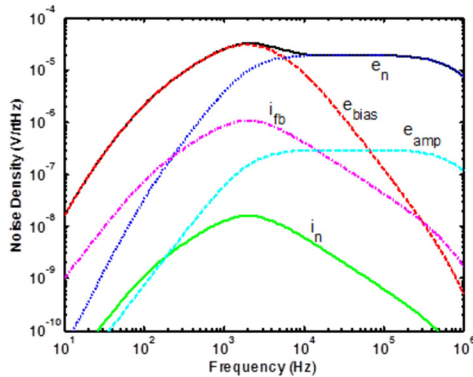

FIG. 10. (Color online) Results of noise computations showing (left) relative contributions of the noise sources to the noise power spectral density (right) comparison of the total predicted noise to the measured noise density.

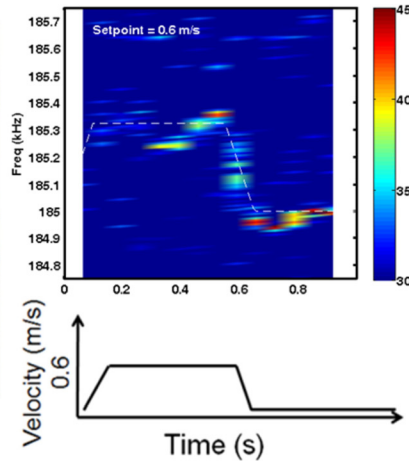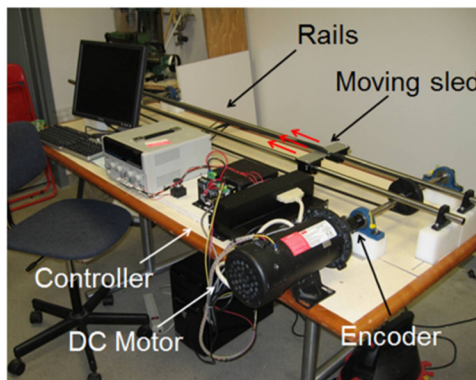Shin et al.: Micromachined Doppler ultrasound array chip

FIG. 11. (Color online) Experimental setup for velocity test (left), and an example spectrogram and sled velocity command (right).

acoustic wave at 185 kHz was sent from the transmitter while the sled accelerated toward the receiver, held at a constant velocity, and then decelerated back to a stop. The controller controls the velocity and distance of the sled, communicating with the dc motor.

The receiver output voltage was recorded for 1 s during each test with a sampling rate of 500 kHz. The sled velocity command accelerates for 0.1 s, holds a constant velocity for 0.45 s, decelerates for 0.1 s, and then stays stopped for the remaining 0.35 s. The controller attempts to follow this velocity set point, feeding back off the shaft encoder. Spectrograms were computed from the received cMUT signal using a short time Fourier transform. A Hamming window with 50% overlap was used to window the data in each time window. Time windows consisting of 2^{16} data points were used, resulting in windows that were 0.13 s long.

Figure 11 shows an example spectrogram as time runs for a particular speed (0.6 m/s), and a sketch of the corresponding expected frequency shift as computed from the commanded sled velocity profile. A Doppler shift is clearly seen, following the shape of the velocity profile. There is

some spread of velocities during the motion, due to the fluctuation of the sled velocity about the set point.

Figure 12 shows similar spectrograms as the commanded velocity of the sled changes between 0.2 and 1 m/s. The Doppler shift increases as the velocity of the sled increases. A good match is obtained between the measured Doppler shift and velocity of the transmitter. The dynamics of the sled motion are apparent in the spectrograms; overshoot, undershoot, and oscillation about the set point can be seen. This appears to be a real velocity variation of the sled. Figure 13 shows the average and standard deviation (as vertical error bars) of measured velocity of the sled as computed from the Doppler shift for each test. The measurement is compared, via the dashed line, to the nominal velocity of the sled. The averages and standard deviations were computed by taking the peak frequency from the spectrogram at 6 times between 0.2 and 0.5 s. The horizontal error bars indicate the maximum and minimum velocity of the sled as determined from shaft encoder data in a second run. The Doppler system appears to accurately measure sled velocity, within the uncertainty in the velocity, which is due primarily to real sled velocity fluctuations during the run.
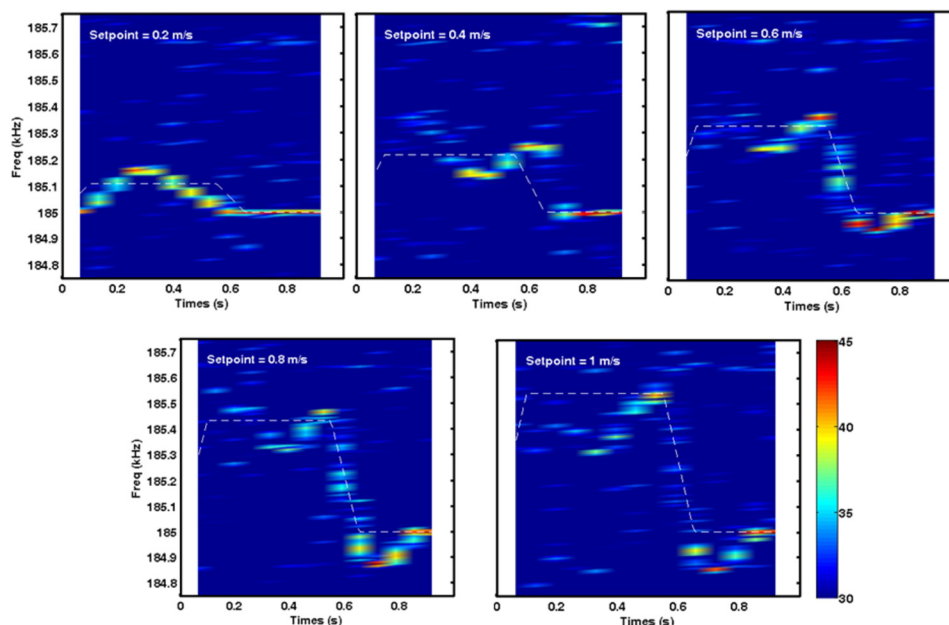

FIG. 12. (Color online) Spectrograms of the shifted signal during different velocity tests. Results are plotted in dB re 1 μV^2/Hz. White dashed lines show the expected frequency based on the sled velocity set point.
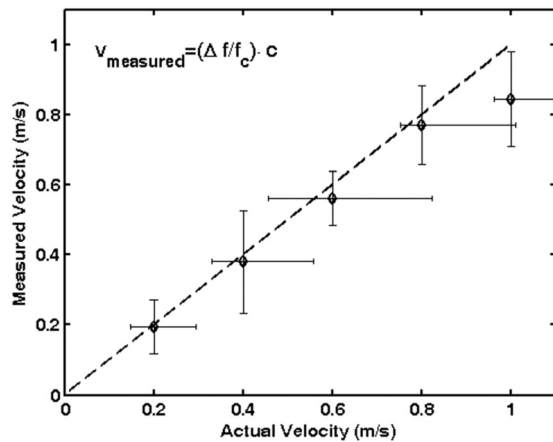
FIG. 13. Comparison of measured and commanded velocity during the nominally constant velocity portion of the motion (from $t = 0.2$ to $t = 0.5$ s). The plotted point is the velocity as computed from the mean detected frequency for each set point. The horizontal error bars span the maximum to minimum velocity for each run as determined from shaft encoder data. The vertical error bars span one standard deviation of detected frequency above and below the mean.

V. CONCLUSION

An in-air acoustic Doppler velocity measurement system using MEMS cMUT array technology was developed and characterized with a variety of experiments. The array operates at 185 kHz and is 1 cm^2 in size. LDV measurements demonstrate that the membrane displacement at center point is 0.4 nm/V^2 at 185 kHz. Beampattern measurements show a $13°$ -3 dB (half power) beam width ($6.5°$ either side of center). The side lobes are 15 dB below the main lobe. These results are all in good agreement with theoretical models. Experimental results for reflected acoustic CW transmit and receive using two chips reflecting off a flat aluminum plate show a maximum range of 60 cm (30 cm out and 30 cm back). Electronic noise in the preamplifier dominates the noise spectrum, and is well modeled using an op-amp noise model. A velocity sled was constructed and used to demonstrate measureable Doppler shifts at velocities from 0.2 to 1.0 m/s. The Doppler shifts agree well with the expected frequency shifts over this range. The major challenges for a system of this type appear to be range limitations. Future work will focus on optimizing the sensor and electronics to increase the signal-to-noise ratio for increased range, particularly by reducing sensor stray capacitance to reduce electronic noise sources in the preamplifier.

ACKNOWLEDGMENTS

[1]G. Hueber, T. Ostermann, T. Bauernfeind, R. Raschhofer, and R. Hagelauer, "New approach of ultrasonic distance measurement technique in robot applications," in *Proceedings of the 5th International Conference on Signal Processing*, pp. 2066–2069 (2000).

[2]Y. Ando and S. Yuta, "Following a wall by an autonomous mobile robot with a sonar-ring," in *Proceedings of the IEEE International Conference on Robotics and Automation*, pp. 2599–2606 (1995).

[3]J. A. Castellanos, J. M. Martinez, J. Neira, and J. D. Tardos, "Simultaneous map building and localization for mobile robots: A multisensor fusion approach," in *Proceedings of the IEEE International Conference on Robotics and Automation*, pp. 1244–1249 (1998).

[4]K. J. Kyriakopoulos and G. C. Anousaki, "Simultaneous localization and map building for mobile robot navigation," IEEE Rob. Autom. Mag. **6**, 42–53 (1999).

[5]C. Y. Lee, H. G. Choi, J. S. Park, K. Y. Park, and S. R. Lee, "Collision avoidance by the fusion of different beam-width ultrasonic sensors," in *Proceedings of IEEE Sensors*, pp. 985–988 (2007).

[6]O. Manolov, S. Noikov, P. Bison, and G. Trainito, "Indoor mobile robot control for environment information gleaning," in *Proceedings of the IEEE Intelligent Vehicles Symposium*, pp. 602–607 (2000).

[7]S. E. C. Biber, E. Shenk, and J. Stempeck, "The Polaroid ultrasonic ranging system," in *Proceedings of the 67th Audio Engineering Society Convention* (1980).

[8]M. I. Haller and B. T. Khuri-Yakub, "1-3 composites for ultrasonic air transducers," in *Proceedings of the IEEE Ultrasonics Symposium*, pp. 937–939 (1992).

[9]R. Przybyla, S. Shelton, A. Guedes, I. Izyumin, M. Kline, D. Horsley, and B. Boser, "In-air range finding with an AlN piezoelectric micromachined ultrasound transducer," IEEE Sensors J. **11**, 2690–2697 (2011).

[10]M. I. Haller and B. T. Khuri-Yakub, "A surface micromachined electrostatic ultrasonic air transducer," in *Proceedings of the IEEE Ultrasonics Symposium*, pp. 1241–1244 (1994).

[11]M. I. Haller and B. T. Khuri-Yakub, "A surface micromachined electrostatic ultrasonic air transducer," IEEE Trans. Ultrason. Ferroelectr. Freq. Control **43**, 1–6 (1996).

[12]O. Ahrens, A. Buhrdorf, D. Hohlfeld, L. Tebje, and J. Binder, "Fabrication of gap-optimized CMUT," IEEE Trans. Ultrason. Ferroelectr. Freq. Control **49**, 1321–1329 (2002).

[13]C. B. Doody, C. Xiaoyang, C. A. Rich, D. F. Lemmerhirt, and R. D. White, "Modeling and characterization of CMOS-fabricated capacitive micromachined ultrasound transducers," J. Microelectromech. Syst. **20**, 104–118 (2011).

[14]P. C. Eccardt, K. Niederer, T. Scheiter, and C. Hierold, "Surface micromachined ultrasound transducers in CMOS technology," in *Proceedings of the IEEE Ultrasonics Symposium*, pp. 959–962 (1996).

[15]I. Ladabaum, X. Jin, H. T. Soh, A. Atalar, and B. T. Khuri-Yakub, "Surface micromachined capacitive ultrasonic transducers," IEEE Trans. Ultrason. Ferroelectr. Freq. Control **45**, 678–690 (1998).

[16]G. Caliano, R. Carotenuto, A. Caronti, and M. Pappalardo, "cMUT echographic probes: Design and fabrication process," in *Proceedings of the IEEE Ultrasonics Symposium*, pp. 1067–1070 (2002).

[17]X. Zhuang, I. Wygant, D. S. Lin, M. Kupnik, O. Oralkan, and B. Khuri-Yakub, "Wafer bonded 2-D CMUT arrays incorporating through-wafer trench-isolated interconnects with a supporting frame," IEEE Trans. Ultrason. Ferroelectr. Freq. Control **56**, 182–192 (2009).

[18]M. J. Madou, *Fundamentals of Microfabrication: The Science of Miniaturization* (CRC Press, Boca Raton, FL, 2002), 294 pp.

[19]M. Bauccio, *ASM Metals Reference Book*, 3rd ed. (ASM International, Materials Park, OH, 1993), 154 pp.

[20]W. N. Sharpe, Jr., in *The MEMS Handbook*, edited by M. Gad-el-Hak (CRC Press, Boca Raton, FL, 2002), 24 pp.

[21]B. Rashidian and M. G. Allen, "Electrothermal microactuators based on dielectric loss heating," in *Proceedings of the 6th IEEE Micro Electro Mechanical Systems Conference*, MEMS'93, Atlanta, GA, pp. 24–29 (1993).

[22]H. Gercek, "Poisson's ratio values for rocks," Int. J. Rock Mech. Min. Sci. **44**, 1–13 (2007).

[23]C. Mastrangelo, "Adhesion-related failure mechanisms in micromechanical devices," Tribol. Lett. **3**, 223–238 (1997).

[24]L. L. Beranek, *Acoustics*, 1996 ed. (Acoustical Society of America, New York, NY, 1996), pp. 47–177.

[25]M. Greenspan, "Piston radiator: Some extensions of the theory," J. Acoust. Soc. Am. **65**, 608–621 (1979).

[26]M. Lax, "The effect of radiation on the vibrations of a circular diaphragm," J. Acoust. Soc. Am. **16**, 5–13 (1944).

[27]Z. Skvor, "On acoustical resistance due to viscous losses in the air gap of electrostatic transducers," Acustica **19**, 295–297 (1967).

[28]D. Homentcovschi and R. N. Miles, "Viscous damping of perforated planar micromechanical structures," Sens. Actuators, A **119**, 544–552 (2005).

[29]B. Carter, in *Op Amps for Everyone*, 2nd ed., edited by R. Mancini (Elsevier, NY, 2003), pp. 138–139.